Search for sphalerons in the $e\mu$ final state at $\sqrt{s} = 13\,\text{TeV}$ with the CMS experiment

von

Florian Rehbein

Bachelorarbeit in Physik

vorgelegt der

Fakultät für Mathematik, Informatik und Naturwissenschaften
der RWTH Aachen

im August 2018

angefertigt im

III. Physikalisches Institut A

bei

Prof. Dr. Thomas Hebbeker

Abstract

This thesis is concerned with the first ever search for electroweak sphalerons in the electron-muon final state in proton-proton collisions at the LHC at a centre-of-mass energy of $\sqrt{s} = 13\,\text{TeV}$. The used data was collected with the CMS experiment in 2016 and sums up to an integrated luminosity of $35.9\,\text{fb}^{-1}$. As no significant deviation from the simulated Standard Model background is observed, an upper limit of 2.22 is set on the fraction of quark-quark interactions above the sphaleron energy threshold of 9 TeV that undergo sphaleron transitions. Furthermore, both the statistical benefits and the emerging issues of various sphaleron-specific event selection criteria are discussed.

Kurzdarstellung

Diese Arbeit beschäftigt sich mit der Suche nach elektroschwachen Sphaleronen in Proton-Proton Kollisionen am LHC bei einer Schwerpunktsenergie von $\sqrt{s} = 13\,\text{TeV}$. Dabei werden Endzustände mit einem Elektron und einem Muon untersucht. Die betrachteten Daten wurden im Jahr 2016 bei einer integrierten Luminosität von $35.9\,\text{fb}^{-1}$ mit dem CMS Experiment gesammelt. Da keine signifikante Abweichung vom simulierten Standardmodell-Untergrund beobachtet wird, kann ein oberes Limit von 2.22 auf den Anteil derjeniger Quark-Quark Wechselwirkungen über der Sphaleron-Potentialbarriere von 9 TeV, welche in Sphaleron-Übergängen resultieren, berachtet werden. Des Weiteren werden verschiedene von der Signalcharakteristik inspirierte Auswahlkriterien, deren statistischer Nutzen und aufkommende Probleme diskutiert.

Contents

1 Theoretical Background

1.1 Standard Model of Particle Physics

The Standard Model (SM) of particle physics is a theoretical framework that combines the current knowledge about elementary particles and their interactions. Because it cannot only explain significant parts of particle physics, but could also correctly predict a wide range of new particles and phenomena in the past, it is the most complete description of the fundamental structure of matter. This section outlines its essential elements, based on [1].

Figure 1.1 gives a first overview on all known elementary particles. They can be classified into two sorts of particles, fermions (particles with half-integer spin) and bosons (integer spin). The SM fermions are further separated into quarks and leptons. Bosons can be attributed to either scalar bosons (spin 0) or vector bosons (spin 1). To each SM particle, one can allocate an antiparticle of the same mass but opposite physical charges.

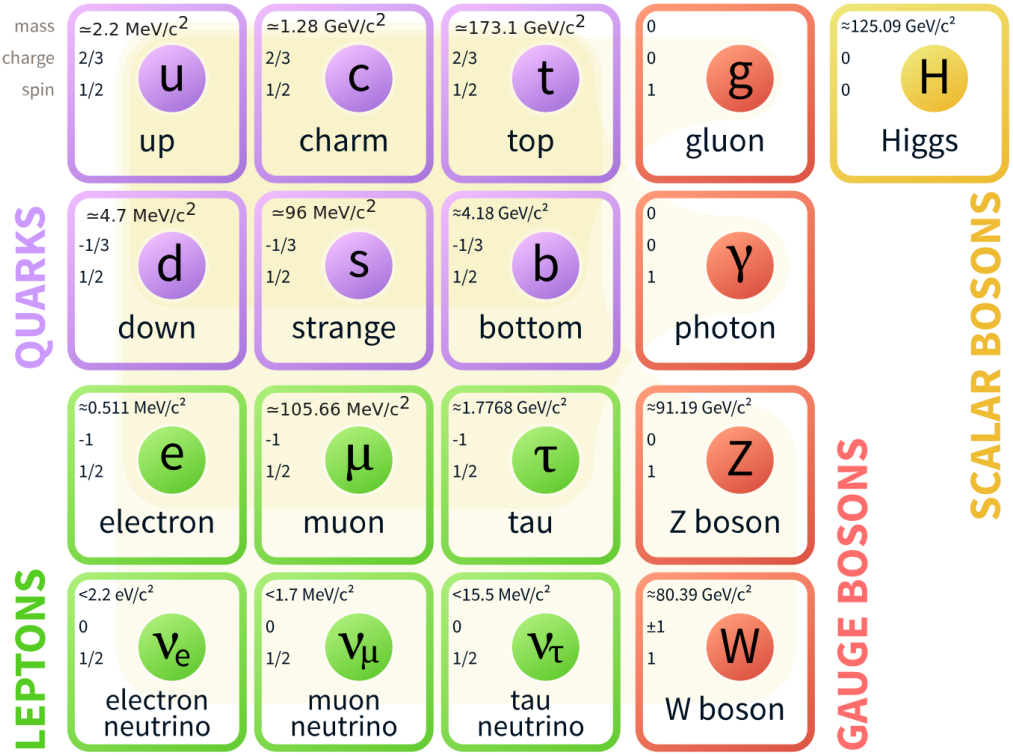

Figure 1.1: Overview on the SM particles [2]

1.1.1 Matter Particles

The SM fermions are made up of six leptons and six quarks, which each are related in generations of two particles. Unlike leptons, quarks carry color charge and therefore participate in the strong interaction.

The three quark generations are formed by the up and down quark in the first, the charm and strange quark in the second and the top and bottom quark in the third generation. The first-mentioned quark of each pair has the electric charge $\frac{2}{3}$; the second one carries the charge $-\frac{1}{3}$. In nature, quarks are either bound together as mesons (quark-antiquark pair) or hadrons (3 quarks) such as protons and neutrons. LHCb, one of the four detectors at the LHC (see section 2.1), was able to detect other, more exotic configurations of mesons and hadrons such as tetraquarks [3] and pentaquarks [4].

Similar to quarks, leptons are divided into three generations, the electron, the muon and the tau, which each is paired together with its respective neutrino. As neutrinos do not carry electric charge (and neither color charge as they rank among the leptons), they only interact via the weak interaction, which is the reason why they can hardly be detected.

1.1.2 Fundamental Interactions and Carrier Particles

The gauge bosons carry the forces of the three fundamental interactions united in the SM: the weak, strong and electromagnetic interaction (see table 1.1). The strength of each interaction can be quantified by their coupling constant, commonly labeled α, which represents the strength of the coupling between the respective gauge boson and the interacting particles.

Table 1.1: Fundamental interactions in the Standard Model

Interaction	Couples to	Carrier particles	Mass [GeV]	relative coupling strength
weak	weak hypercharge	$W^{\pm}$	80.39	10^{-6}
		Z	91.19	
electromagnetic	electric charge	Photon	0	$\frac{1}{137}$
strong	color charge	8 gluons	0	1

The massless photon couples to all particles with electric charge and is the exchange particle of the electromagnetic interaction. Putting it into relation, it is about two orders of magnitude weaker than the strong interaction ($\frac{\alpha_{EM}}{\alpha_S} \approx \frac{1}{137}$). As the photon is massless, the electromagnetic interaction operates on an infinite range.

All particles carry weak hypercharge, which is the charge of the weak interaction. Hence, all particles interact weakly. Mediators of the weak force are the electrically charged $W^{\pm}$-bosons and the electrically neutral Z-boson. Due to their big mass, the weak interaction

operates on a short range of around 10^{-17} m. As its name suggests, it is about six orders of magnitudes weaker than the strong interaction ($\frac{\alpha_W}{\alpha_S} \sim 10^{-6}$) and therefore the weakest of the fundamental SM forces. The electromagnetic and the weak interaction are unified in the electroweak (EW) theory.

Particles carrying color charge interact strongly by exchange of gluons. There are three possible colors (red, green, blue) and three corresponding anticolors. In total there are eight gluons which all carry color charge and therefore interact strongly themselves (self-coupling). It operates at distances smaller than about 10^{-15} m. One would naturally expect nine gluons, as gluons carry color and anticolor and there are three colors. However, the singlet state does not interact with other color states and therefore does not exist.

Gravitation, however, the fourth fundamental interaction, cannot be described by the Standard Model. While this is a significant shortcoming of the Standard Model, it still applies at small scales because of the weak coupling of the gravitational force ($\frac{\alpha_G}{\alpha_S} \sim 10^{-39}$).

1.1.3 Higgs Mechanism

The only spinless SM boson (scalar boson), the Higgs boson, couples to every massive particle, whereby the coupling strength is proportional to the particles' mass. This so-called Higgs mechanism essentially gives the particles their respective mass. As the Higgs boson was initially proposed theoretically and later experimentally discovered by CMS and ATLAS [5], it is one of the reasons of the success of the Standard Model.

1.2 Sphaleron Processes

The sphaleron (Greek: ready to fall) is a static, unstable, and finite-energy non-perturbative solution of the electroweak sector of the Standard Model [6]. It can be seen as a transition between two vacuum states. An interesting property of sphaleron transitions is the violation of the baryon number B and lepton number L while preserving $B - L$.

The electroweak theory leads to a nontrivial vacuum structure with an infinite number of ground states. These ground states can be enumerated by the so-called Chern-Simons number N_{CS} [7]. The periodic potential of the SM ground state can be seen in figure 1.2.

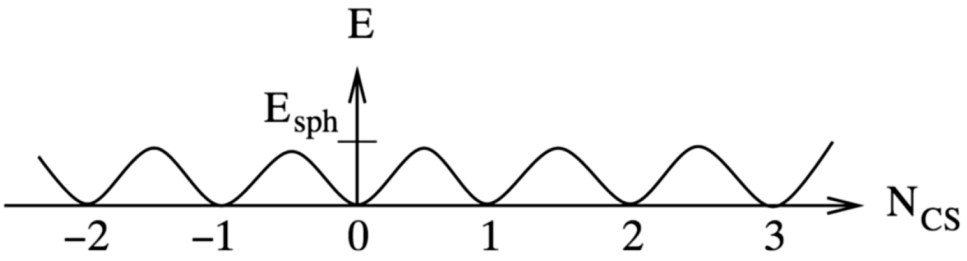

Figure 1.2: The periodic sphaleron potential in the electroweak theory. [8]

The degeneration of the vacuum indicates that our universe is sitting in one of the minima of the potential corresponding to a specific Chern-Simons number N_{CS} [9]. The classical transition to an adjacent minimum over the potential barrier with height E_{sph} is called

sphaleron.

In the theoretical framework of the electroweak theory, one can calculate, based on the values of the EW couplings, the value of the barrier height to be around $E_{sph} \approx 9\,TeV$. Even if this energy is within reach of the LHC, the sphaleron transition rate was thought to be highly suppressed by the large potential barrier, as the probability for two partons to overcome this threshold is very low. However, S.-H. Henry Tye and Sam S. C. Wong stated in a recent paper [10], that sphaleron transitions can be observed even at collision energies $\sqrt{s} < E_{sph}$ at LHC. They justify this claim with the periodic nature of the Chern-Simons potential which leads to a band structure for transitions through the sphaleron barrier and ultimately results in a reduced suppression.

As already mentioned, sphaleron transitions are related to a change in the Chern-Simons number ΔN_{CS} and thereby change each the baryon number B and the lepton number L by $3\Delta N_{CS}$. This factor 3 results from a change in the lepton number for each lepton doublet by ΔN_{CS}. The same applies to quarks, as the baryon number changes by ΔN_{CS} for each of the three quark generations [11]. Taken together, the following applies:

$$\Delta\,(B - L) = 0 \tag{1.2.1}$$

$$\Delta\,(B + L) = 6 \cdot \Delta N_{CS} \tag{1.2.2}$$

A sphaleron process in proton-proton collisions at the LHC could proceed as shown in equation 1.2.3 below:

$$u + u \rightarrow e^{+}\mu^{+}\tau^{+}\bar{t}\,\bar{t}\bar{b}\,\bar{c}\,\bar{c}\,\bar{s}\,\bar{d} + X \tag{1.2.3}$$

This process is an example of a possible sphaleron transition with $\Delta N_{CS} = -1$ [12].

The change of the baryon number and lepton number in sphaleron transitions is a significant characteristic, as these two quantities are conserved in every other SM process that could be observed until now. This opens up the possibility of understanding the matter-antimatter asymmetry, which is still an unsolved mystery in physics.
This asymmetry can be enumerated via the asymmetry parameter [13]

$$\frac{n_B - n_{\overline{B}}}{n_\gamma} \approx 6.1 \times 10^{-10} \tag{1.2.4}$$

with the (anti)baryon density n_B ($n_{\overline{B}}$) and the photon density n_γ.
As this number is non-zero, in the early universe more baryons than antibaryons were formed. This process, called baryogenesis, could not be finally explained as there are different theories possibly explaining the asymmetry. However, the sphaleron reflects an interesting approach, as it is described within the Standard Model and the potential barrier with its high energy to reach with particle colliders such as the LHC, would have been easy to overcome at the high temperatures prevalent in the early universe [14].

2 Experimental Setup

2.1 Large Hadron Collider (LHC)

The Large Hadron Collider (LHC), the world's largest particle collider, was installed by the European Organization for Nuclear Research (CERN) around 100 metres below the French-Swiss border area near Geneva. Producing proton-proton collisions at a centre-of-mass energy of currently up to $\sqrt{s} = 13\,\text{TeV}$, the LHC runs at higher energies than any other collider and hence is expected to give a deeper look into particle physics.

After being pre-accelerated by one linear and three circular accelerators, the proton bunches enter the LHC, which itself has a circumference of about 27 km [15]. The proton bunches then are accelerated even further until they reach energies up to 6.5 TeV and collide at one of four collision points, which each is surrounded by ultramodern particle detectors, namely ATLAS, ALICE, CMS, and LHCb. An overview of the location of the detectors and the LHC itself is given in figure 2.1.

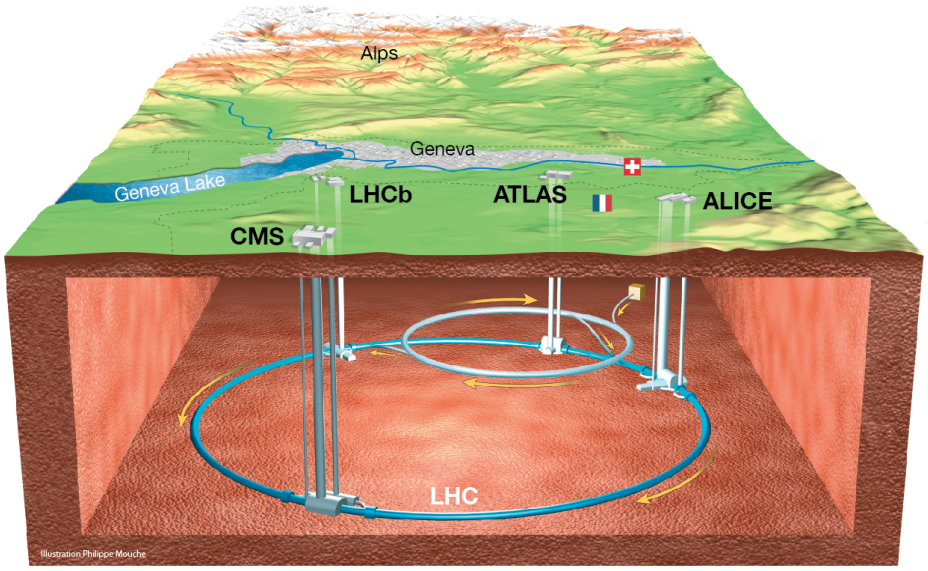

Figure 2.1: Overview of the LHC and its four complex detectors ATLAS, ALICE, CMS and LHCb [16]

This analysis takes a look at the dataset recorded by the Compact Muon Solenoid (CMS) detector in 2016. In 2016 the CMS detector collected data with an integrated luminosity of $40.96\,\text{fb}^{-1}$ [17] (the concept of luminosity will be explained in section 2.3) at a centre-of-mass energy of $\sqrt{s} = 13\,\text{TeV}$.

2.2 Compact Muon Solenoid (CMS)

As already mentioned before, the Compact Muon Solenoid (CMS) detector sits at one of the four collision points of the LHC. If not stated otherwise, the information given in this section was taken from [18]. Overall, the detector is 15 metres high, 21 metres long and weighs about 14,000 tonnes. Being a general-purpose detector, the CMS is designed to provide the possibility of observing a wide range of new physics phenomena. Figure 2.2 gives a look inside the detector and shows the different layers around the collision point. The detector is structured into the rotationally symmetric barrel section and two endcaps. In the following, a short overview on the different layers and their function is given, starting at the core element of the detector, the superconducting solenoid magnet.

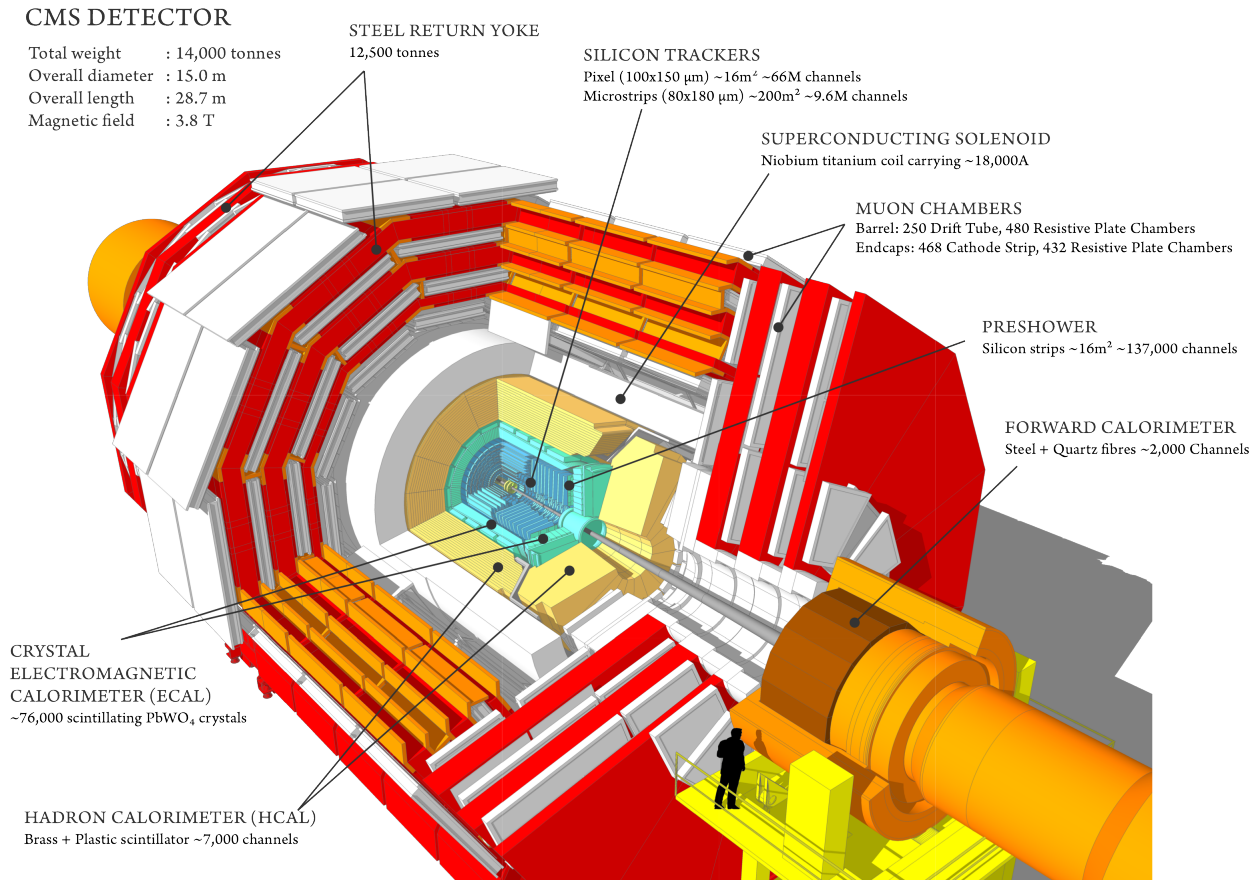

Figure 2.2: CMS detector [19]

2.2.1 Superconducting Magnet

The powerful solenoid magnet is formed by a coil of superconducting wire and generates a homogeneous magnetic field of around 4 tesla. This magnetic field bends charged particles' trajectories and thereby allows measuring their momentum. An essential part of the magnet is the iron yoke, which is made up of three layers interleaving the muon chambers. It closes the magnetic flux and works as a filter for the muon system as only muons and neutrinos traverse the thick iron layer [20].

2.2.2 Inner Tracking System

The inner tracking system is the innermost layer of the detector and has the purpose of measuring the trajectories of charged particles precisely and efficiently. It consists of a pixel detector with three barrel layers and a silicon strip tracker with ten barrel layers. Each endcap consists of 2 disks in the pixel detector and 12 disks in the strip tracker. With a pixel size of $100 \times 150\,\mu\text{m}^2$ and a typical cell size of $10\,\text{cm} \times 80\,\text{mm}$ for the silicon stripes, each measurement with the inner tracking system is accurate to $10\,\mu\text{m}$. The reconstruction of the trajectories, which are bend due to the homogeneous magnetic field inside the tracker, allows measurement of the momentum and the electric charge of charged particles such as electrons and hadrons.

2.2.3 Electromagnetic Calorimeter

The electromagnetic calorimeter (ECAL) is the next outer layer of the detector and measures the energy of electromagnetic interacting particles such as electrons and photons. It is formed by almost $80,000$ lead tungstate ($PbWO_4$) crystals that are used for their high density and short radiation length. Travelling through the crystal, electrons emit high energy photons via bremsstrahlung, which then, as well as the photons originally produced in the collision, produce electron/positron pairs and so on. This process is called electromagnetic shower and leads the traversing electrons and photons into depositing their total energy in the ECAL. Thereby optical photons are produced, which are detected by photodetectors glued to the ends of the crystals, and as the amount of these photons is proportional to the energy deposit, one can measure the energy of the particles [21].

2.2.4 Hadron Calorimeter

Hadrons, which are particles made of quarks and gluons such as kaons and pions, pass through the ECAL, although they deposit a part of their energy on their way. This results in need of the hadronic calorimeter (HCAL). It is made of alternating layers of plastic scintillators and brass, working as an absorber material. Surpassing the absorber material, the hadrons produce secondary particles which ultimately end up producing optical photons in the scintillator material and thus allow an energy measurement of the hadrons. Hence in principle, the HCAL measures the strongly interacting hadrons like the ECAL measures electrons and photons.

2.2.5 Muon System

Another important part of the CMS experiment is the name giving muon system, which builds the outermost layer of the detector. In order to guarantee a high momentum resolution, the muon system makes up a major part of the detectors size. The barrel region contains drift chambers with standard rectangular drift cells. As the muon rate (and background rate as well) is very low in this region, there is no need for an extremely fast response time. In the endcap regions, due to the high muon rate and high background levels, CMS uses cathode strip chambers which stand out for their fast response time and radiation resistance. Both chamber types (drift champers and cathode strip chambers) are based on the same detection principle. If a muon passes such a chamber, it ionizes gas atoms. The thereby released electrons can be detected, and one can reconstruct the path of the muon.

When also taking the tracker into consideration, CMS can measure the momentum of high momenta muons (above 1 TeV) with a resolution of about 5 %.

2.3 Important Quantities

In this section, a consistent coordinate system as well as important quantities, that are frequently used in this analysis, are introduced and defined.

The origin of the coordinate system is set at the collision point inside the beam pipe, the x-axis points to the center of the LHC ring, the y-axis is orientated vertically upward and the z-axis is in the direction of the beam.

Rather than using the polar angle θ it is the convention to use the so-called pseudorapidity η, which is defined as

$$\eta = -\ln\left(\tan\left(\frac{\theta}{2}\right)\right). \tag{2.3.1}$$

The motivation behind this variable transformation is, that differences in the pseudorapidity are invariant under Lorentz boosts. As η and the azimuthal angle ϕ are orthogonal coordinates, one can define the angular separation between two particles as

$$\Delta R = \sqrt{(\Delta\eta)^2 + (\Delta\phi)^2}. \tag{2.3.2}$$

Another essential quantity which will appear in this analysis is the invariant mass. Using natural units, where $\hbar = c = 1$, it can be calculated via

$$M = \sqrt{\left(\sum_i E_i\right)^2 - \left(\sum_i \vec{p}_i\right)^2} \tag{2.3.3}$$

with energy E and momentum $\vec{p}$ of the considered particles. Additionally, the transverse momentum

$$p_T = \sqrt{p_x^2 + p_y^2} \tag{2.3.4}$$

appears in this analysis.

A very important quantity in connection with particle colliders is the concept of luminosity. The luminosity $\mathcal{L}$ is an accelerator characteristic and indicates the expected event rate $\dot{\mathrm{N}}$ of a process with cross section σ:

$$\dot{\mathrm{N}} = \sigma \cdot \mathcal{L} \tag{2.3.5}$$

At the LHC, where two bunches containing n_1 and n_2 particles, collide with frequency f, the luminosity can be calculated via

$$\mathcal{L} = f\frac{n_1 n_2}{4\pi\sigma_x\sigma_y} \tag{2.3.6}$$

whereby σ_x and σ_y measure the size of the Gaussian beam profile in x- and y-direction [22]. Integrating the luminosity over time leads to the integrated luminosity:

$$\mathcal{L}_{int} = \int \mathcal{L}\,\mathrm{d}t \tag{2.3.7}$$

3 Datasets and Monte Carlo Samples

3.1 Datasets

This analysis is based on data recorded with the CMS detector in 2016 at $\sqrt{s} = 13\,\text{TeV}$. The SingleMuon and SinglePhoton datastreams (Run B-H) are used, the reconstruction version derives from 3rd February 2017. The amount of data sums up to an integrated luminosity of $35.9\,\text{fb}^{-1}$.

3.2 Signal Simulation

The sphaleron signal samples are generated at LO with the `BARYOGEN v1.0` generator [23]. The parton distribution thereby is simulated with the `CT10 LO PDF` [24] set.
This analysis uses three different samples generated at different values of the barrier height $\text{E}_{\text{sph}} = 8, 9, 10\,\text{TeV}$. These samples have already been used in an approved CMS publication in [12].

This work uses the notation introduced in [12]:

$$\sigma = \text{PEF} \cdot \sigma_0 \tag{3.2.1}$$

with the total cross section σ, the pre-exponential factor PEF and the cross section parameter σ_0. As the value of the PEF, defined as the fraction of quark-quark interactions above the sphaleron energy threshold E_{sph} that undergo the sphaleron transition, is unknown, the cross section for sphaleron production is unknown as well. The values of σ_0, which can be calculated, are given in table 3.1.

Table 3.1: Values of the cross section parameter σ_0 for the given sphaleron energy thresholds E_{sph} taken from [11].

E_{sph} [TeV]	σ_0 [fb]
8	121
9	10.1
10	0.51

3.3 Background Simulation

As there is a number of well-known SM processes which produce (or fake) the $e\mu$ final state, one has to simulate these background processes in order to differentiate the sphaleron signal.

Table 3.2 and table 3.3 list the used Monte Carlo samples. They include the name of the used generator, kinematic cuts, and information about the cross section σ of the respective process.
As one can add any number of loops and vertices to the Feynman diagram of each process, the cross section is calculated up to a certain accuracy, given by its order. The leading order (LO) includes all Feynman diagrams in the leading order of the coupling constant of the interaction (see section 1.1.2). Taking into account all Feynman diagrams within the next order of the coupling constant, one talks of next-to-leading order (NLO), and so on.
It is important to know that there are samples, where the cross section is multiplied by the so-called k-factor, which adjusts the cross section of the sample to a calculated cross section of a higher order.

Table 3.2: List of the background Monte Carlo samples

Process	Generator	Kinematic cuts [GeV]	σ [pb]	k-factor	Order
$t\bar{t}$					
$t\bar{t} \to 2\ell 2\nu$	POWHEG	$M_{\ell\ell} < 500$	87.31	-	NNLO
$t\bar{t} \to 2\ell 2\nu$	POWHEG	$500 < M_{\ell\ell} < 800$	0.286	1.116	NNLO
$t\bar{t} \to 2\ell 2\nu$	POWHEG	$800 < M_{\ell\ell} < 1200$	0.02864	1.116	NNLO
$t\bar{t} \to 2\ell 2\nu$	POWHEG	$1200 < M_{\ell\ell} < 1800$	0.002677	1.116	NNLO
$t\bar{t} \to 2\ell 2\nu$	POWHEG	$M_{\ell\ell} > 1800$	0.0001533	1.116	NNLO
Diboson					
$WW \to \ell\nu qq$	POWHEG	-	49.997	-	NNLO
$WW \to 4q$	POWHEG	-	51.723	-	NNLO
$WW \to 2\ell 2\nu$	POWHEG	$M_{\ell\ell} < 200$	12.178	-	NNLO
$WW \to 2\ell 2\nu$	POWHEG	$200 < M_{\ell\ell} < 600$	1.39	-	NNLO
$WW \to 2\ell 2\nu$	POWHEG	$600 < M_{\ell\ell} < 1200$	0.057	-	NNLO
$WW \to 2\ell 2\nu$	POWHEG	$1200 < M_{\ell\ell} < 2500$	0.0036	-	NNLO
$WW \to 2\ell 2\nu$	POWHEG	$M_{\ell\ell} > 2500$	0.000054	-	NNLO
$WZ \to 3\ell\nu$	POWHEG	-	4.42965	-	NLO
$ZZ \to 4\ell$	POWHEG	-	1.256	-	NLO
$ZZ \to 2\ell 2\nu$	POWHEG	-	0.564	-	NLO
Single top					
tq (t channel)	POWHEG	-	136.02	-	NNLO
$\bar{t}q$ (t channel)	POWHEG	-	80.95	-	NNLO
$tW \to 2\ell 2\nu b$	POWHEG	-	19.3	-	NNLO
$\bar{t}W \to 2\ell 2\nu \bar{b}$	POWHEG	-	19.3	-	NNLO
$tq/\bar{t}q \to \ell\nu bq/\bar{b}q$ (s channel)	aMC@NLO	-	3.36	-	NLO

Table 3.3: List of the background Monte Carlo samples

Process	Generator	Kinematic cuts [GeV]	σ [pb]	k-factor	Order
Drell-Yan					
$Z \to \mu\mu$	POWHEG	$50 < M_{\mu\mu} < 120$	1975	-	NLO
$Z \to \mu\mu$	POWHEG	$120 < M_{\mu\mu} < 200$	19.32	-	NLO
$Z \to \mu\mu$	POWHEG	$200 < M_{\mu\mu} < 400$	2.731	-	NLO
$Z \to \mu\mu$	POWHEG	$400 < M_{\mu\mu} < 800$	0.241	-	NLO
$Z \to \mu\mu$	POWHEG	$800 < M_{\mu\mu} < 1400$	0.01678	-	NLO
$Z \to \mu\mu$	POWHEG	$1400 < M_{\mu\mu} < 2300$	0.00139	-	NLO
$Z \to \mu\mu$	POWHEG	$2300 < M_{\mu\mu} < 3500$	$8.948 \cdot 10^{-5}$	-	NLO
$Z \to \mu\mu$	POWHEG	$3500 < M_{\mu\mu} < 4500$	$4.135 \cdot 10^{-6}$	-	NLO
$Z \to \mu\mu$	POWHEG	$4500 < M_{\mu\mu} < 6000$	$4.56 \cdot 10^{-7}$	-	NLO
$Z \to \mu\mu$	POWHEG	$6000 < M_{\mu\mu}$	$2.066 \cdot 10^{-8}$	-	NLO
$Z \to ee$	POWHEG	$50 < M_{ee} < 120$	1975	-	NLO
$Z \to ee$	POWHEG	$120 < M_{ee} < 200$	19.32	-	NLO
$Z \to ee$	POWHEG	$200 < M_{ee} < 400$	2.731	-	NLO
$Z \to ee$	POWHEG	$400 < M_{ee} < 800$	0.241	-	NLO
$Z \to ee$	POWHEG	$800 < M_{ee} < 1400$	0.01678	-	NLO
$Z \to ee$	POWHEG	$1400 < M_{ee} < 2300$	0.00139	-	NLO
$Z \to ee$	POWHEG	$2300 < M_{ee} < 3500$	$8.948 \cdot 10^{-5}$	-	NLO
$Z \to ee$	POWHEG	$3500 < M_{ee} < 4500$	$4.135 \cdot 10^{-6}$	-	NLO
$Z \to ee$	POWHEG	$4500 < M_{ee} < 6000$	$4.56 \cdot 10^{-7}$	-	NLO
$Z \to ee$	POWHEG	$6000 < M_{ee}$	$2.066 \cdot 10^{-8}$	-	NLO
$Z \to \tau\tau \to e\mu$	aMC@NLO	-	1867	-	NLO
Wγ					
$W\gamma \to \ell\nu\gamma$	MadGraph	$p_T^\gamma < 500$	405.271	1.2066	NLO
$W\gamma \to \ell\nu\gamma$	MadGraph	$p_T^\gamma > 500$	0.012	1.2066	NLO
Wjets					
$W(\ell\nu) + jets$	MadGraph	$H_T < 100$	50690	-	NNLO
$W(\ell\nu) + jets$	MadGraph	$100 < H_T < 200$	1292.0	-	NNLO
$W(\ell\nu) + jets$	MadGraph	$200 < H_T < 400$	385.9	-	NNLO
$W(\ell\nu) + jets$	MadGraph	$400 < H_T < 600$	47.9	-	NNLO
$W(\ell\nu) + jets$	MadGraph	$600 < H_T < 800$	12.8	-	NNLO
$W(\ell\nu) + jets$	MadGraph	$800 < H_T < 1200$	5.261	-	NNLO
$W(\ell\nu) + jets$	MadGraph	$1200 < H_T < 2500$	1.334	-	NNLO
$W(\ell\nu) + jets$	MadGraph	$H_T > 2500$	0.03089	-	NNLO
QCD					
QCD	PYTHIA8	$20 < p_T < 30$	2960198	-	LO
QCD	PYTHIA8	$30 < p_T < 50$	1652471	-	LO
QCD	PYTHIA8	$50 < p_T < 80$	437504	-	LO
QCD	PYTHIA8	$80 < p_T < 120$	106033	-	LO
QCD	PYTHIA8	$120 < p_T < 170$	25190.5	-	LO
QCD	PYTHIA8	$170 < p_T < 300$	8654.49	-	LO
QCD	PYTHIA8	$300 < p_T < 470$	797.35	-	LO
QCD	PYTHIA8	$470 < p_T < 600$	79.026	-	LO
QCD	PYTHIA8	$600 < p_T < 800$	25.095	-	LO
QCD	PYTHIA8	$800 < p_T < 1000$	4.707	-	LO
QCD	PYTHIA8	$p_T > 1000$	1.621	-	LO

3.3.1 Top-antitop pair production ($t\bar{t}$)

In this process, a top-antitop pair is produced. As a result of their short lifetime, the top quarks decay into a b quark and a W boson before they can hadronise. The W bosons then further decay into an electron or a muon respectively and its corresponding neutrino. The Feynman diagram of such a process can be seen in figure 3.1.

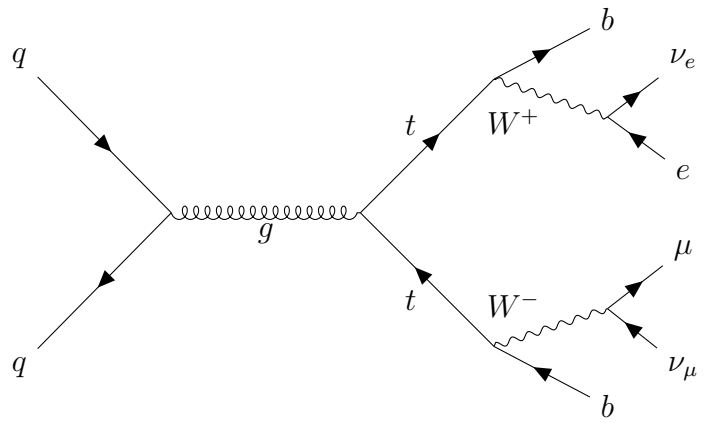

Figure 3.1: Exemplary Feynman diagram of the top-antitop pair production. Both generated W bosons decay leptonically, producing an $e\mu$ final state.

3.3.2 Single top production

Processes, where a single top quark along with a W boson or other quarks is produced, can cause an $e\mu$ final state. The Feynman diagram of such a process is shown in figure 3.2.

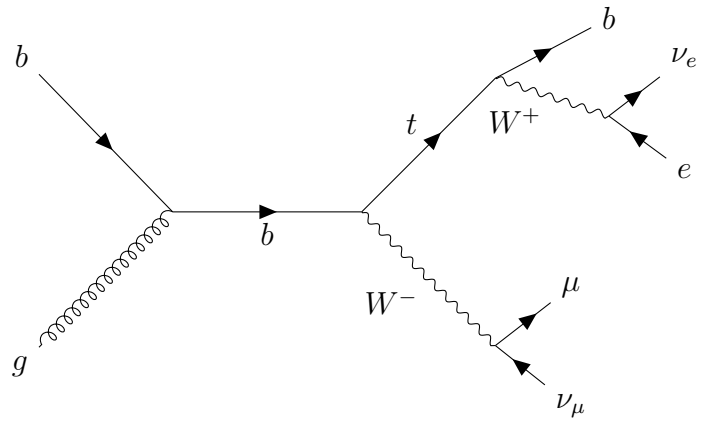

Figure 3.2: Exemplary Feynman diagram of the single top background: Both emitted W bosons (by the bottom and the top quark) decay leptonically and produce an $e\mu$ final state.

3.3.3 W boson pair production (WW)

As shown in figure 3.3, this background describes the production of two W bosons, which both decay leptonically into an electron with its corresponding neutrino and a muon with its corresponding neutrino respectively.

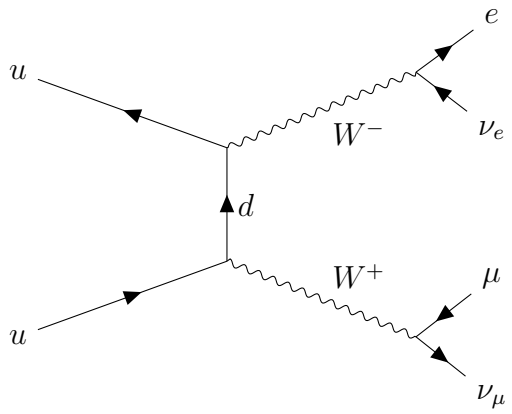

Figure 3.3: Exemplary Feynman diagram of the W boson pair production. Both bosons decay leptonically.

3.3.4 Diboson production including Z bosons (WZ, ZZ)

This background describes processes similar to the W boson pair production, but with one or two Z bosons produced instead of W bosons, which further decay into lepton-antilepton pairs and hence can produce an $e\mu$ final state. Two exemplary Feynman diagrams are shown in figure 3.4.

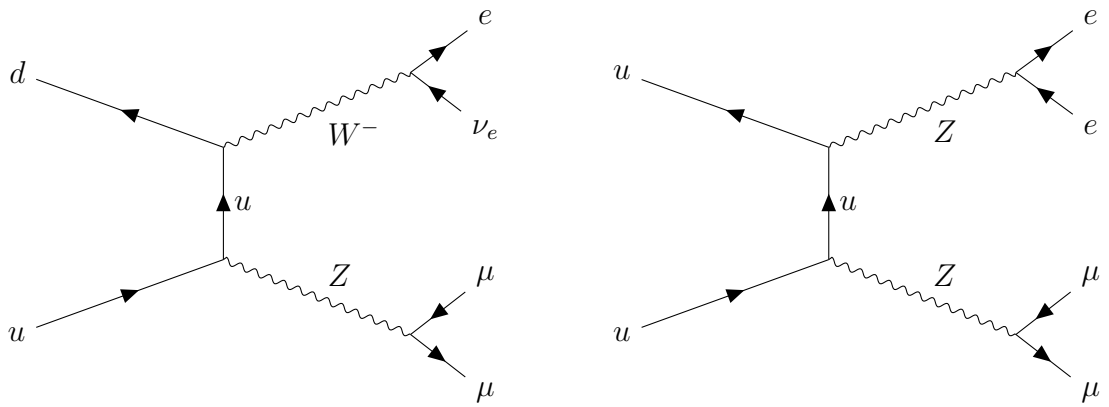

(a) WZ production **(b)** ZZ production

Figure 3.4: Exemplary Feynman diagram of diboson production including Z bosons. The Z bosons decay into a lepton-antilepton pair and therefore lead to additional leptons in the final state.

3.3.5 Drell-Yan processes

This background describes the emission of a Z boson or a virtual photon in the course of quark-antiquark annihilation. As shown in figure 3.5, this Z boson or photon then further decays into two leptons of the same generation but opposite charge. Hence Drell-Yan processes cannot produce an $e\mu$ final state. However, there are two possibilities of measuring such a final state with the detector. Firstly, two τ leptons can be produced, which can decay into an electron and a muon respectively so that the $e\mu$ final state ultimately is produced.
Secondly, it is possible to measure the sought-after final state by misidentification of one of the produced leptons.

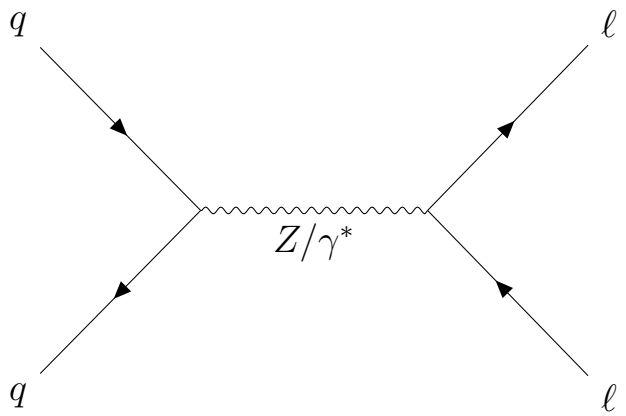

Figure 3.5: Exemplary Feynman diagram of a Drell-Yan process. Two quarks annihilate and emit a Z boson or a virtual photon, which then further decays into a lepton-antilepton pair.

3.3.6 QCD processes

Quantum chromodynamics (QCD) processes produce hadronic jets, which can fake an $e\mu$ final state. This process can be seen in figure 3.6.

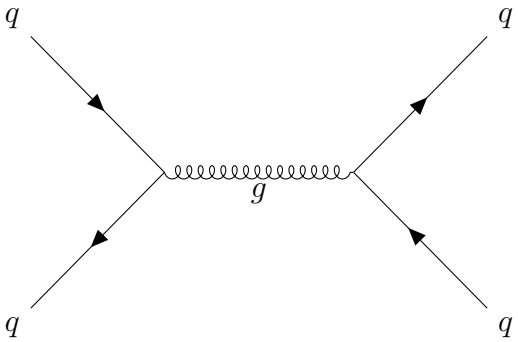

Figure 3.6: Feynman diagram of a QCD process. A quark-antiquark pair annihilates and emits a gluon which further decays into a quark-antiquark pair.

3.3.7 W+jets

This background includes processes, that produce a leptonically decaying W boson and hadronic jet(s). As hadronic jets can fake electrons and muons, this processes can fake the $e\mu$ final state. An exemplary Feynman diagram is given in figure 3.7.

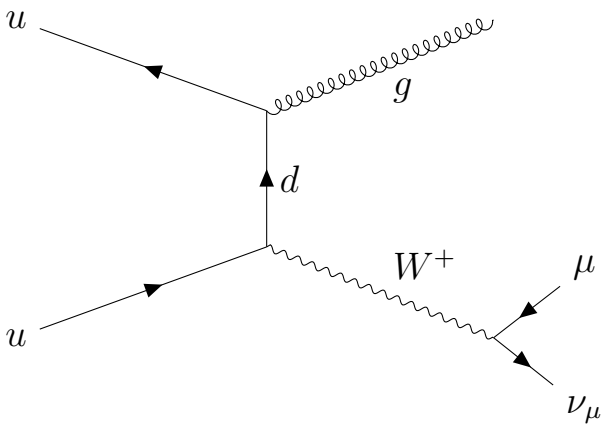

Figure 3.7: Exemplary Feynman diagram of the W+jets background. The emitted W boson decays leptonically. Additionally, a gluon, causing a hadronic jet, is emitted in the shown process.

3.3.8 Wγ

Processes as the one shown in figure 3.8 can fake the $e\mu$ final state if the generated photon is misidentified as an electron and the W boson decays leptonically into a muon and a muon neutrino. As the photon is much more likely to fake an electron as to fake a muon, similar processes where the W boson decays into an electron are negligible.

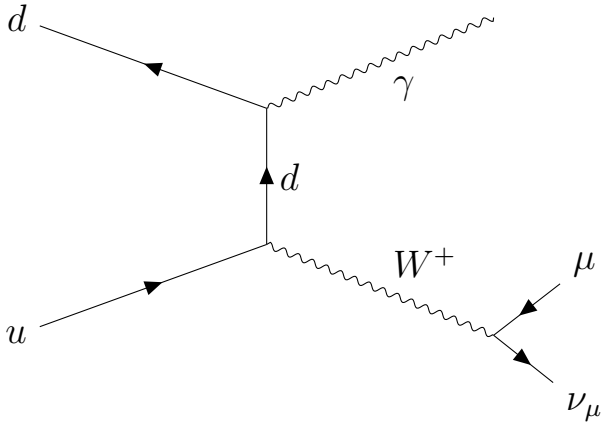

Figure 3.8: Exemplary Feynman diagram of the Wγ background. Similar to the W+jets background, the emitted W boson decays leptonically into either an electron or a muon (and the corresponding neutrino). Additionally, a photon is emitted, which can be misidentified as an electron.

4 Event Selection

4.1 Trigger

In order to select good events, a high energy muon and a high energy photon trigger, linked with a logical *OR*, are used. Namely, this analysis uses the `HLT_Mu50_v` trigger path with a muon p_T threshold of 50 GeV and the `HLT_Photon175_` trigger path with a photon p_T threshold of 175 GeV.

4.2 Muon Identification

In order to select the muon candidates, the high-p_T muon ID recommended by the Muon Physics Object Group [25] for muons with $p_T > 200$ GeV, is used. It includes the selection criteria listed below:

- The muon candidate has to be reconstructed as a global muon.
- The reconstructed global-muon track must include at least one muon chamber hit, which suppresses hadronic punch-through (leakage of hadron cascades through the absorber [26]) and muons from decays in flight.
- In order to suppress punch-through and accidental track-to-segment matches, there have to be muon segments in at least two muon stations.
- The p_T relative error of the muon best track has to be less than 30%.
- To suppress cosmic muons and further suppress muons from decays in flight, the muons tracker path must have a transverse impact parameter d_{xy} smaller than 2 mm with respect to the primary vertex. Additionally, one requires the longitudinal distance of the tracker track with respect to the primary vertex d_z to be less than 5 mm.
- For the purpose of further suppressing muons from decays in flight, there has to be at least one pixel hit.
- As the p_T measurement is realized via reconstructing the muon path, the muon candidates have to hit at least 5 tracker layers in order to obtain a good p_T measurement.

Additionally, as recommended in [25], for 2016 data and the applied high-p_T muon trigger, only muons with $p_T > 53$ GeV within $|\eta| < 2.4$ were selected.

4.3 Electron Identification

The electron candidates are selected using the High Energy Electron Positron identification (HEEP ID) version 7.0 recommended by the CMS EGamma Physics Object Group [27]. Table 4.1 completely lists the associated selection cuts. It displays different cuts for the different regions in the detector (barrel/endcap) that were introduced in section 2. The variables, which have not been declared so far but yet appear in this table, are therefore introduced in the list below, using information taken from [28].

Table 4.1: Electron identification criteria (HEEP v7.0)

Variable	Barrel	Endcap
E_T	$> 35\,\text{GeV}$	$> 35\,\text{GeV}$
η range	$\lvert\eta_{SC}\rvert < 1.4442$	$1.566 < \lvert\eta_{SC}\rvert < 2.5$
isEcalDriven	$= 1$	$= 1$
$\lvert\Delta\eta_{in}^{seed}\rvert$	< 0.004	< 0.006
$\lvert\Delta\phi_{in}\rvert$	< 0.06	< 0.06
H/E	$< 1/E + 0.05$	$< 5/E + 0.05$
full $5 \times 5\,\sigma_{i\eta i\eta}$	-	< 0.03
full $5 \times 5\,E^{2\times5}/E^{5\times5}$	> 0.94 OR $E^{1\times5}/E^{5\times5} > 0.83$	-
EM+HAD Depth 1 Isolation	$< 2 + 0.03E_T + 0.28\rho$	$< 2.5 + 0.28\rho$ for $E_T < 50\,\text{GeV}$ $< 2.5 + 0.03(E_T - 50) + 0.28\rho$ else
Track Isolation: Trk Pt	< 5	< 5
Inner Layer Lost Hits	$\leqslant 1$	$\leqslant 1$
$\lvert d_{xy}\rvert$	< 0.02	< 0.05

- $|\Delta\eta_{in}^{seed}|$: This variable is defined as the difference in η between the supercluster position in the ECAL and the track direction at the innermost layer of the tracker system.
- $|\Delta\phi_{in}|$: Similarly describes the difference in ϕ.
- H/E: The ratio of energy measured in the HCAL (in a $\Delta R = 0.15$ cone around the electron seed), over the energy measured in the ECAL.
- $5 \times 5\,\sigma_{i\eta i\eta}$: This denotes the spread in η of the electron's energy in the 5×5 block around the seed crystal.
- $5 \times 5\,E^{2\times5}/E^{5\times5}$: The ratio of energy deposited in the highest energy 2×5 block over the energy in the 5×5 block around the seed crystal.
- EM+HAD Depth 1 Isolation: Electromagnetic and hadronic isolation of the electron candidate. Precisely, it defines the sum of transverse energies of neutral electromagnetic candidates and hadronic candidates, respectively, in a $\Delta R = 0.3$ cone around the electron, divided by the electrons transverse momentum.

- Track Isolation: This denotes the ratio of the p_T sum of all particles in a $\Delta R = 0.3$ cone around the electron over the electron p_T.
- Inner Layer Lost Hits: Number of times the reconstructed electron trajectory intersects tracker material without a hit.

4.4 Kinematic Cuts

Even if the LHC is capable of producing sphalerons, the event rate is expected to be reasonably low as a consequence of the large potential barrier $E_{sph} \approx 9\,\text{TeV}$. Hence the significant number of background processes producing the sought-after $e\mu$ final state makes it difficult to identify possible sphaleron transitions. Kinematic cuts on analysis level are used to increase the signal to background ratio and therefore improve the statistical significance of the collected data.

The basic idea of this event selection is to look for kinematic characteristics of the signal that stand out from the background. As the simulation of sphaleron-induced processes is fraught with great uncertainty, a number of kinematic cuts are discussed in this section, not only to increase the signal to background ratio but also to better understand the characteristics of the used sphaleron MC samples.

4.4.1 Number of Jets

In section 1.2 it was already shown that sphaleron transitions entail a large number of particles in the final state. The process presented in equation 1.2.3 which, amongst other particles, includes seven quarks, works as an example. As quarks (and emitted gluons) cause hadronic jets, one would expect to observe many jets in sphaleron-induced transitions. The number of reconstructed jets for the collected data, the expected background and the signal sample is shown in figure 4.1. It should be noted that exemplarily the sample generated at $E_{sph} = 9\,\text{TeV}$ is shown, as the samples generated at 8 TeV and 10 TeV show the same characteristics.

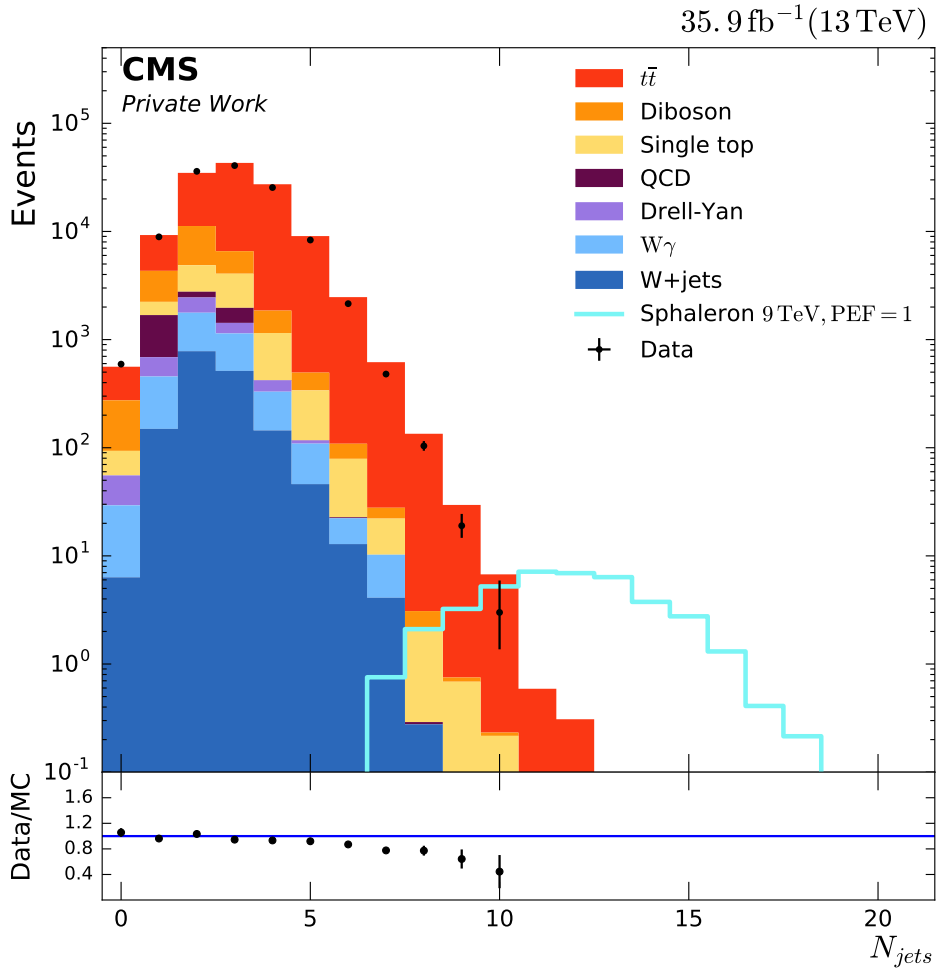

Figure 4.1: Distribution of the number of reconstructed jets. One can see the sphaleron signal to peak at a higher number of jets than the estimated background and the recorded data.

One can observe a good agreement between data and background. As expected, the sphaleron signal shows a large number of jets, peaking at around 12. As the background on the other hand peaks at 3 jets, implementing a minimum value of jets can drastically improve the signal to background ratio.

As a consequence of the characteristics shown in figure 4.1, this analysis implements a $N_{jets} > 6$ cut. This cut drastically suppresses the background while reducing the signal only to a small extent.

4.4.2 Electric Charge

Another interesting quantity to look at is the electric charge of the electron and the muon. Theoretically, one would expect two leptons generated from a sphaleron transition to have the same electric charge, as the lepton number L changes by $\Delta L = \pm 3$ and the simplest variant would be three leptons or three antileptons in the final state.

However, sphaleron transitions could also look like the process shown below:

$$u + u \to e^+e^+e^-\mu^+\tau^+ + \bar{t}\,\bar{t}\bar{b}\,\bar{c}\,\bar{c}\,\bar{s}\,\bar{d} + X \tag{4.4.1}$$

This process does not violate any of the characteristics introduced in section 1.2 but includes a positively charged antimuon and a negatively charged electron in the final state. Thus in principle, sphaleron transitions allow both equally and oppositely charged leptons to be produced.

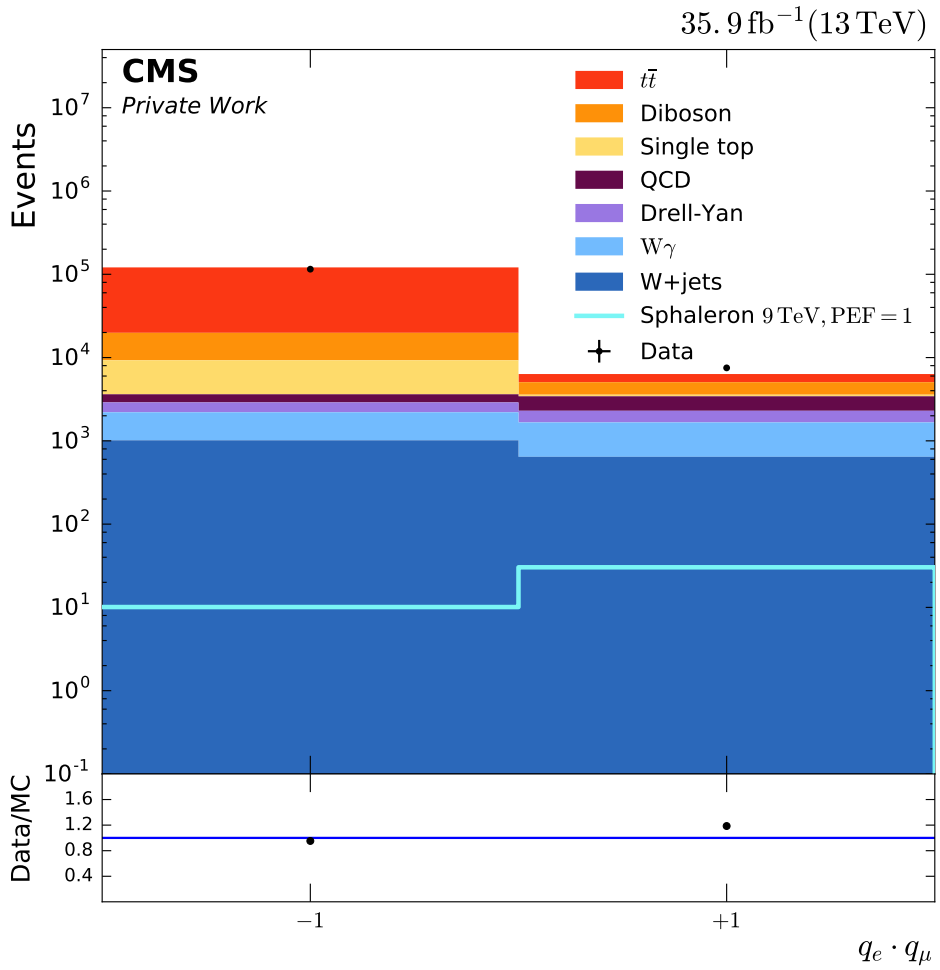

Figure 4.2: This distribution shows the product of the electric charge of the electron and the muon, which is either +1 if they have the same charge or −1 in case of opposite charge.

Figure 4.2 shows the product of the electric charges of the electron and the muon. The following applies:

$$q_e \cdot q_\mu = \begin{cases} -1 & \text{opposite electric charge} \\ +1 & \text{same electric charge} \end{cases} \tag{4.4.2}$$

One can see that the underground processes are more likely to produce oppositely charged electrons and muons. As expected, the fake backgrounds such as QCD are equally distributed as the fake rate of leptons and antileptons should be the same.

The sphaleron samples, on the other hand, consist more equally charged electrons and

muons in the final state. As a consequence, a same electric charge will be required in this analysis as another kinematic cut.

4.4.3 $\Delta\phi\,(e\mu)$

As the colliding protons travel through the LHC in the opposite direction at the same beam energy, the rest frame of the collision is equally the rest frame of the CMS detector. Hence, as a result of the conservation of the four-momentum, a two-body decay would result in a back-to-back emission of the two produced particles, which would lead to a difference in the polar angle of $\Delta\phi = \pm\pi$.

Sphaleron transitions, on the other hand, produce a large number of particles which results in the difference of the polar angle to be approximately equally distributed (see figure 4.3).

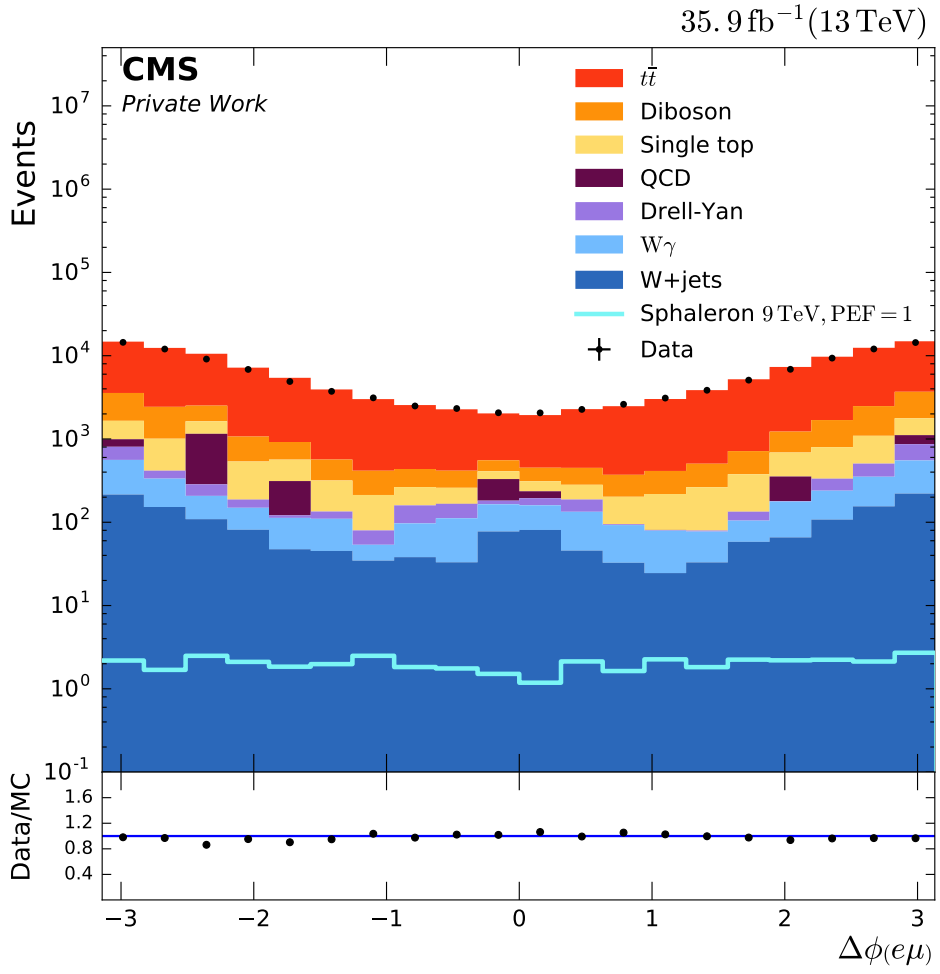

Figure 4.3: Distribution of $\Delta\phi$, the difference in the polar angle, of the electron and the muon. While the sphaleron signal is approximately equally distributed, there are more estimated background events for larger values of $|\Delta\phi|$.

Once again one can find a good agreement between data and background. Unlike the sphaleron signal, they show a larger number of events at larger values of $|\Delta\phi\,(e,\mu)\,|$. This may be reasonable as the background processes on average contain fewer particles in the

final state which leads to an increased probability of the electron and the muon to be emitted in different directions. As a result, limiting the absolute value $|\Delta\phi\,(e,\mu)\,|$ of the spread in the polar angle between the electron and the lepton to a maximum value would further increase the signal to background ratio.

However, this analysis will not implement such a cut in order to decrease the number of sphaleron-induced events not further. This reason will be further explained in section 4.4.4.

4.4.4 Cutflow

Figure 4.4 shows the number of events of the background, data and signal after each applied cut. The first bin, labeled *Preselection*, thereby contains all events that passed the discussed event selection (trigger and identification requirements) except the kinematic cuts.

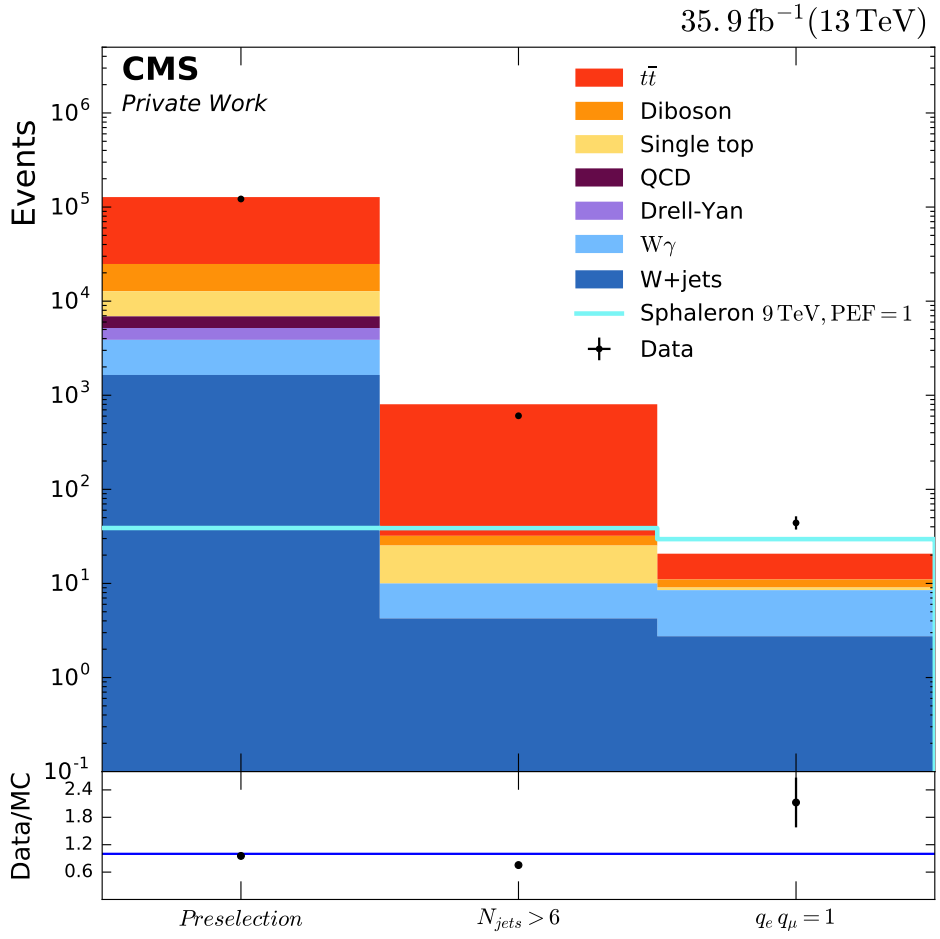

Figure 4.4: Impact of the applied kinematic cuts on the number of events. One can see a drastic reduction of the estimated background while the number of signal events only slightly decreases.

The applied cuts drastically reduce the number of background events by more than 99 %, while only reducing the number of signal events by 24 % (this number applies to the sample

generated at 9 TeV, it is roughly the same for the other samples). This high magnification of the signal to background ratio is the reason for the waiving of additional kinematic cuts such as $|\Delta\phi\,(e\mu)\,|$, as this would lead to the loss of signal events and the signal efficiency (fraction of events surviving all selection criteria, see section 4.5) already is reasonably low.

4.5 Signal Efficiency

In order to take a look at the number of signal events passing the discussed selection criteria, the signal efficiency was calculated at three different stages: branching ratio, acceptance and full selection (also called acceptance×efficiency).

Even if sphaleron transitions contain at least one lepton from each lepton family in the final state, both an electron and a muon are only produced at a certain percentage of all events, as there can also occur neutrinos which CMS cannot detect. This percentage of all generated events that contain one electron and one muon is called branching ratio.

The acceptance is defined as the share of those events that contain an electron and a muon within the acceptance of the CMS detector on generator level. These criteria are given by

$$E_T^e > 35\,\text{GeV}, \quad |\eta^e| < 1.4442 \text{ or } 1.566 < |\eta^e| < 2.5 \tag{4.5.1}$$

for the generated electron and

$$E_T^\mu > 53\,\text{GeV}, \quad |\eta^\mu| < 2.4 \tag{4.5.2}$$

for the generated muon.

The acceptance × efficiency is defined as the ratio of events that fulfill all described selection criteria and pass the kinematic cuts divided by the total number of generated events.

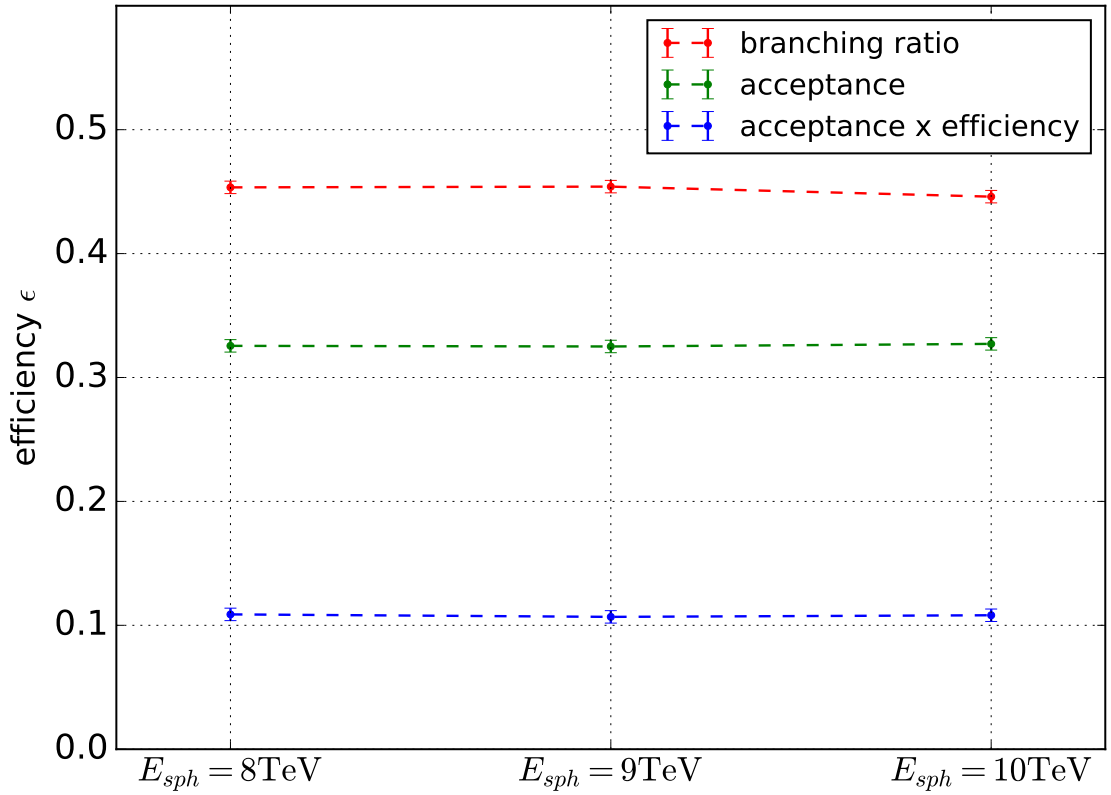

Figure 4.5: Signal efficiency as a function of the potential barrier height E_{sph} of the generated sphaleron samples. The three different samples show very similar efficiencies.

Figure 4.5 shows these quantities for all three generated signal samples at $E_{sph} = 8, 9, 10\,\text{TeV}$. As already mentioned these samples show a very similar behaviour looking at the leptons kinematics. This impression is also confirmed by the fact that the efficiencies are about the same for all samples.
One can see that about 45 % of all generated events contain an electron and muon, while only about 32 % contain an electron and muon within the acceptance of the detector.
Looking at the acceptance × efficiency, slightly more than 10 % reconstructed events of all generated events pass all event selection criteria and ultimately end up in the final result. It should be noted that this loss of events is mainly a result of the reconstruction and identification of the leptons, as the majority of the signal events pass the kinematic cuts (see section 4.4.4).

5 Analysis

5.1 Pile-up Reweighting

At the LHC, not single protons, but bunches of protons collide with each other. As a result, after each bunch crossing on average more than 20 inelastic proton-proton interactions overlap [18], which leads to an increased amount of primary vertices in the event. This effect is called pile-up and can be corrected by reweighting the Monte Carlo samples based on the expected number of primary vertices.
This number can be determined by multiplying the instantaneous luminosity with the minimum bias cross section of 69.2 mb [29], which is an approximation for the total cross section of inelastic proton-proton interactions. Figure 5.1 shows the comparison of the number of primary vertices for the data and background simulation before and after the pile-up reweighting.

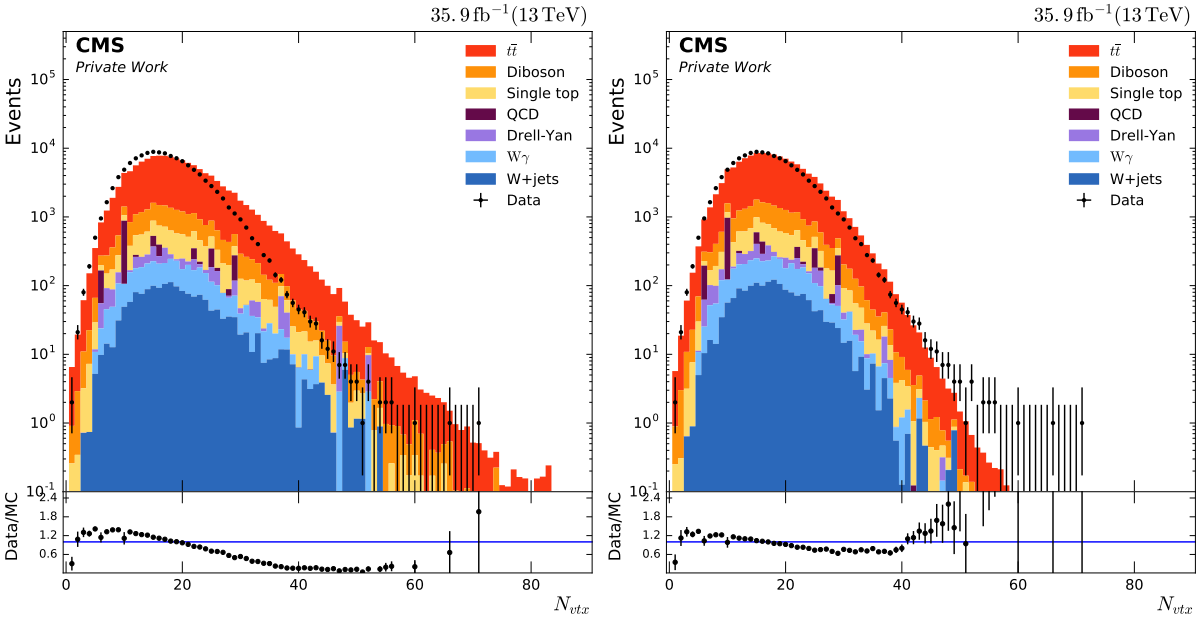

(a) Before pile-up reweighting **(b)** After pile-up reweighting

Figure 5.1: Reconstructed number of vertices. While after the pile-up reweighting data and expected background do not show a perfect agreement, it still improves significantly.

One can see the improvement in agreement between data and background. However, as there is still a systematic shift to higher numbers of primary vertices, the reweighting appears not to work impeccably.

5.2 Systematic Uncertainties

In order to obtain a statistically significant result, estimating the systematic uncertainties that affect the measurement is necessary. This section will discuss the systematic uncertainties influencing the invariant mass distribution of the electron and the muon, which will be ultimately used for the statistical interpretation (see chapter 6).

- Luminosity: The uncertainty of the luminosity from the official measurement, estimated to be 2.5 % [30], is applied in this analysis.
- Pile-up: The minimum biased cross section, which is used for the pile-up reweighting described in section 5.1, is associated with an uncertainty of 4.6 %. This value, as well as the cross section itself, is the result of a best-fit method conducted by the Physics Validation Group [29].
- PDF: An important uncertainty in simulating proton-proton collisions arises from our imperfect knowledge of the structure of the proton [31]. Simulating this inner structure is based on the parton distribution functions (PDF), which is associated with a systematic uncertainty. Following the official recommendation of the PDF4LHC group [32], this uncertainty is estimated by variation of the background estimation with overall 100 replicas of the used PDF set, which results in an uncertainty on the cross section.
- Scale factors: As the detector simulation can differ from actual data representing real physical processes, scale factors for the trigger and identification of the electron and muon as well as the muon isolation are applied. Uncertainties of these scale factors propagate towards a systematic uncertainty on the final distribution.
- Electron E_T scale: Following [33], the uncertainties on the electron energy scale are estimated at 0.4 % in the barrel region and 0.8 % in the endcaps.
- Muon p_T scale: For the muon p_T scale, the transverse curvature of high-p_T muons as a function of η and ϕ is compared between data and MC. Depending on the measured difference, a bias on the curvature is introduced. Further information on this procedure can be found in [34].
- Muon p_T resolution: The muon p_T resolution can be determined with high-p_T cosmic ray muons and is given as 1 % in the barrel and 2 % in the endcaps [35].
- Background cross sections: The process-dependent cross sections contain systematic errors. Following [36], for DY a 2 % uncertainty, for ZZ a 3 % uncertainty, for WZ and WW a 4 % uncertainty and for single top a 5 % uncertainty is used.
  The uncertainty on the Wγ, QCD and W+jets cross sections are estimated at 50 %, as the photon-to-electron and jet misidentification rates highly depend on the MC simulation.

5.3 Invariant Mass Distribution

The invariant mass distribution for all events passing the event selection criteria described in chapter 4 except for the kinematic cuts (section 4.4) can be seen in figure 5.2.

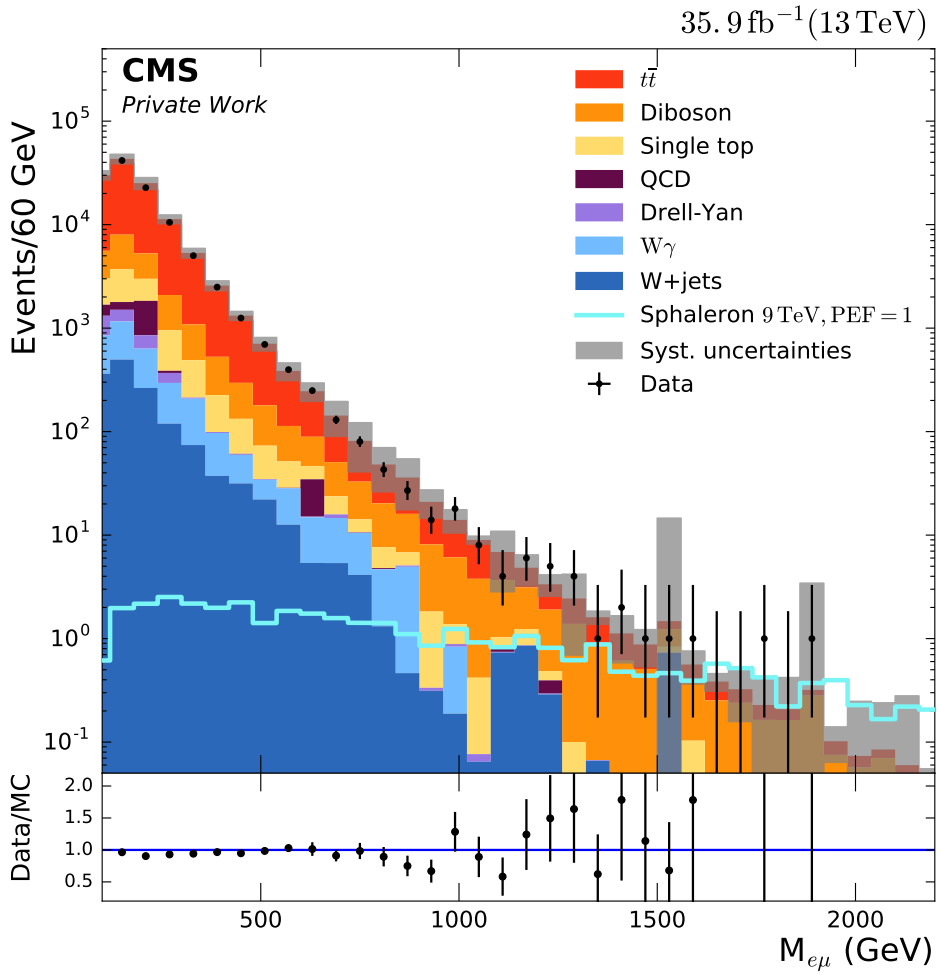

Figure 5.2: Invariant mass distribution including events that pass all selection criteria except for the kinematic cuts on the electric charge or the number of jets. The grey band represents the systematic uncertainties on the background simulation.

The distribution shows a good agreement between the recorded data and the expected SM background. As no significant deviation has been observed, in chapter 6 this distribution is used to calculate limits on the pre-exponential factor PEF of the sphaleron model (see section 3.2).

Figure 5.3 shows the effect of the kinematic cuts discussed in section 4.4 on the invariant mass distribution. The distribution after the cut on the number of jets shows missing background events for small masses $M_{e\mu} < 350\,\text{GeV}$ compared to the recorded data; the distribution of events with only equally charged leptons shows the same characteristic for masses $M_{e\mu} < 1300\,\text{GeV}$. The possible reasons for this disagreement are discussed further below after looking at the final distribution.

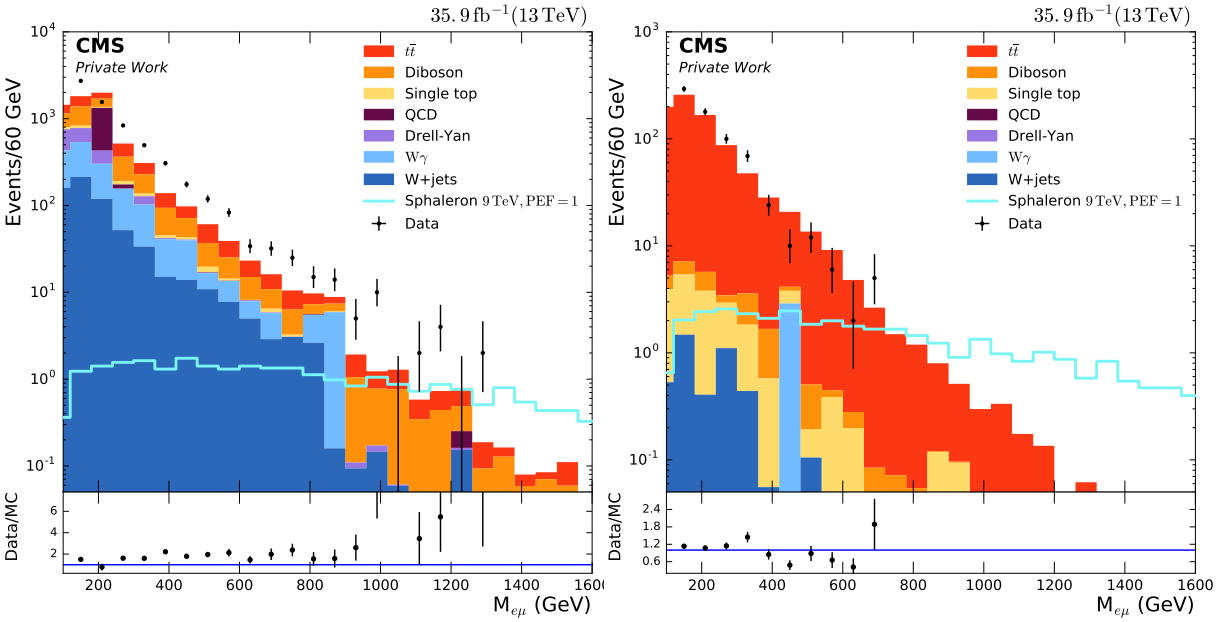

(a) Only events with equally charged electron and muon ($q_e q_\mu = 1$) contribute.

(b) Only events with more than 6 reconstructed jets ($N_{jets} > 6$) contribute.

Figure 5.3: Invariant mass distributions with either one of the two kinematic cuts applied.

The invariant mass distribution with both kinematic cuts applied is shown in figure 5.4. As it shows a disagreement between the recorded data and the estimated background, in the first place one could think of a discovery.
However, the most likely cause for the lack of background events is the inadequate simulation of events with a large number of jets and equally charged leptons.
As it was shown in section 4.4.4, the cuts on the number of jets and the electric charge of the leptons fulfill their purpose of increasing the signal to background ratio. On the downside, Monte Carlo simulations often fall short of generating multi-jet events due to the complexity of those events. For example, in reference [37], the complexity of constructing event generators for multijet final states is discussed.
Another important aspect is a possible mismatch between data and MC samples in incorrectly assigning the leptons electric charge. This means that the misidentification rate of the leptons charge could differ between actual data and generated samples. A similar behaviour was already shown for another quantity in section 5.1, where the discrepancy over reconstructing the number of vertices (pile-up) was discussed.

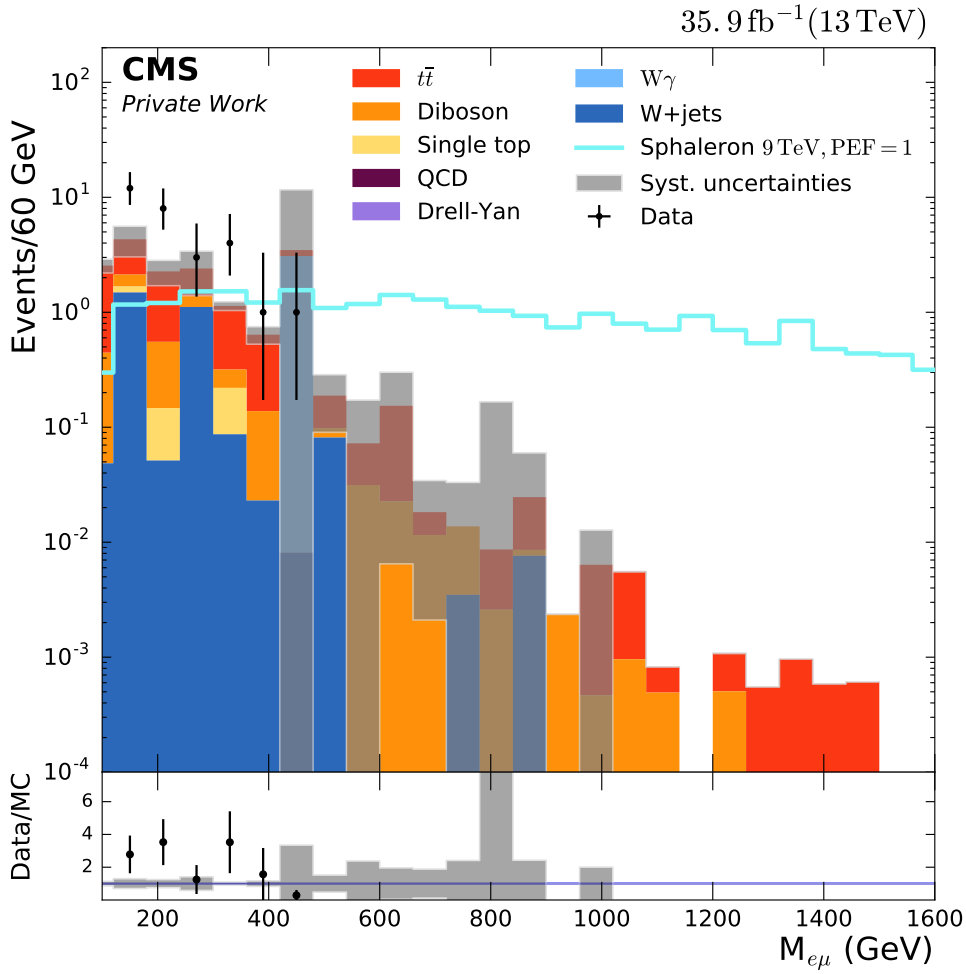

Figure 5.4: Invariant mass distribution of events that pass all selection criteria including the kinematic cuts on the electric charge and the number of jets.

Ultimately this would mean that the observed disagreement is caused by shortcomings of the models used for generating the Monte Carlo samples for the chosen kinematic cuts or non-consideration of relevant background processes. In order to judge whether this is the actual reason for the disagreement, further analysis has to to be performed. This analysis would have to look into the discussed possible shortcomings of the used background simulation. Another possibility would be searching for other selection criteria which already have been proven to show a good agreement between simulation and data.

6 Statistical Interpretation

This chapter discusses a statistical interpretation of the results seen in chapter 5. While the background is significantly reduced by the kinematic cuts, the MC samples faced some problems in this region. For this reason, the observed limit before those cuts is calculated. Additionally, the statistical benefits of signal-specific selection criteria are discussed by calculating expected limits on the PEF using the invariant mass distribution after both kinematic cuts.

6.1 Bayesian Approach

The limit calculation used in this analysis uses the Bayesian approach. It is based on Bayes' theorem, which gives an expression for the probability $P(A|B)$ of A to be true assuming B is true:

$$P(A|B) = \frac{P(B|A)P(A)}{P(B)} \tag{6.1.1}$$

This theorem can be reinterpreted for the use in particle physics by expressing the probability of a hypothesis H to be true given a measured set of data via

$$P(H|data) = \frac{L(data|H)\,\pi(H)}{\int L(data|H')\,\pi(H')\,\mathrm{d}H'}. \tag{6.1.2}$$

Thereby $L(data|H)$ describes the likelihood of observing a set of data assuming the hypothesis to be true and $\pi(H)$ denotes the prior degree of belief, which can, for example, originate from an independent experiment. This analysis assumes a uniformly distributed degree of belief due to a lack of knowledge on the cross section for sphaleron production. Applying this approach on calculating an upper limit on a parameter θ such as the cross section of a hypothetical process (or the PEF in the case of the sphaleron), one can calculate the upper limit θ_{lim} at a certain confidence level CL via

$$\mathrm{CL} = \int_0^{\theta_{lim}} P(\theta|data)\,\mathrm{d}\theta. \tag{6.1.3}$$

A detailed description of the Bayesian approach is given in [38].

6.2 Exclusion Limits

As mentioned in section 5.3, the invariant mass distribution without signal-specific cuts is used for calculating an upper limit on the pre-exponential factor PEF for sphaleron production, as the MC samples seem to properly describe the background. For this purpose, the `Higgs combine tool` [39] is used, which takes the shape of the distribution into account as it approaches the limit calculation binwise.

In the first place this calculation results to an upper limit on the cross section × branching ratio (BR), as sphalerons do not necessarily lead to an $e\mu$ final state. The values of the branching ratio for the used signal samples have already been derived in section 4.5 and therefore allow calculating limits on the total cross section σ for sphaleron production. Applying the cross section parameter σ_0 (see section 3.2), the PEF is given by

$$\mathrm{PEF} = \frac{\sigma}{\sigma_0}. \tag{6.2.1}$$

The resulting exclusion limit on the PEF can be seen in figure 6.1. The dashed black line shows the median expected limit from the background simulation; the solid black line represents the observed limit based on the measured data. The green and yellow bands display the 68 % and 95 % uncertainty bands of the expected limit.

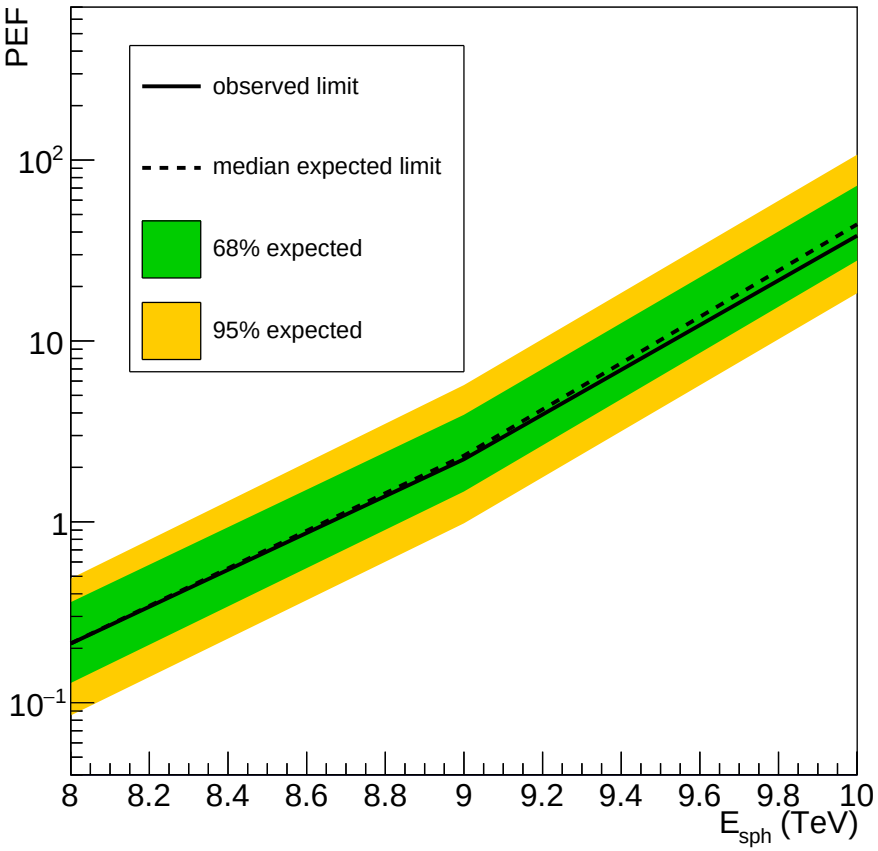

Figure 6.1: Expected and observed upper limit on the sphaleron PEF without signal-specific analysis level cuts.

For the sample generated at $E_{sph} = 9\,\text{TeV}$, which is the calculated value of the potential barrier height for sphaleron production (see section 1.2), an experimental upper limit on the pre-exponential factor of 2.22 is observed.

Analysing events only passing general event selection criteria certainly leaves room for increasing the statistical significance of setting an upper limit on the PEF. The discussed cuts on the number of jets and the lepton charge increased the signal to background ratio but on the other hand, raised issues regarding the background simulation. Assuming that the observed mismatch is actually caused by poor background simulation (for example falsely neglected background processes or inadequate MC generation), one can still calculate an expected limit on the PEF. The result is shown in figure 6.2. Due to the lack of statistics, the calculation is based on the integrated number of events which on the downside leads to non-consideration of the shape of the distribution.

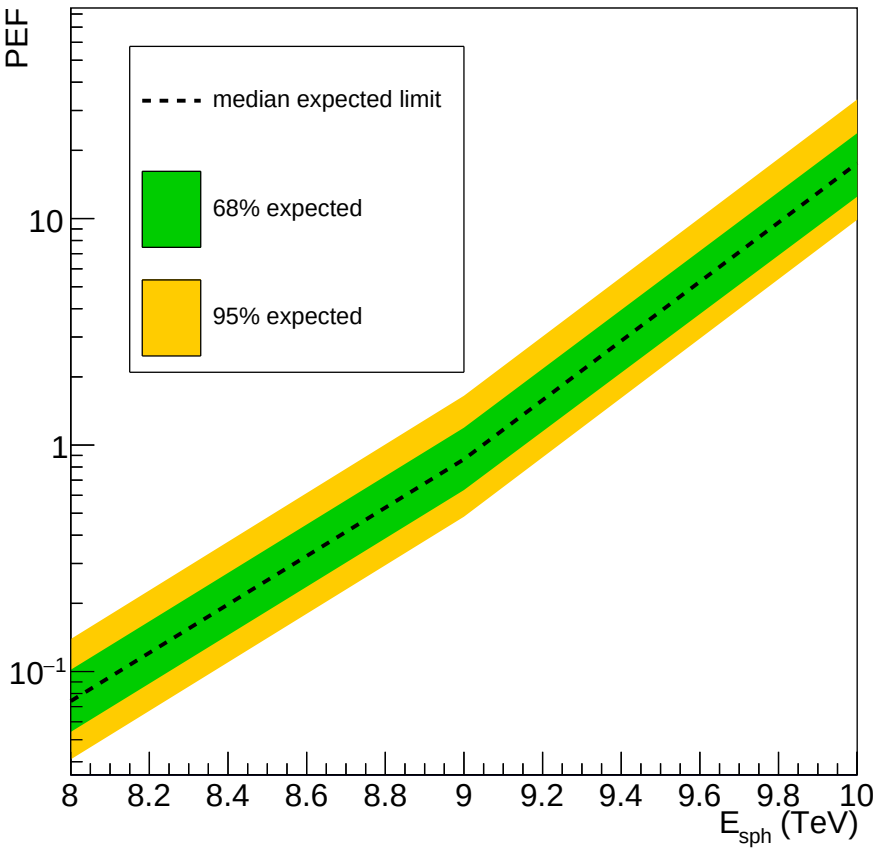

Figure 6.2: Expected upper limit on the sphaleron PEF with signal-specific kinematic cuts.

For the sphaleron transition energy of 9 TeV an expected upper limit on the PEF of 0.86 was calculated. It should be noted that this limit only has the purpose of showing the potential of future searches for sphaleron-specific selection criteria and working on adequate background simulation. It cannot be ruled out that the value of the PEF lies above this expected limit and therefore sphalerons contribute to the distribution. However, being almost three times smaller than the observed exclusion limit, it still shows the statistical benefits of the kinematic cuts on the lepton charge and the number of jets. Assuring adequate simulation of all contributing background processes (which again would require further work), one could either derive a significantly smaller upper limit on the PEF or possibly discover the sought-after sphaleron signal.

7 Conclusion and Outlook

The first search for electroweak sphalerons in the electron-muon final state in proton-proton collisions at the LHC at a centre-of-mass energy of $\sqrt{s} = 13\,\text{TeV}$ has been performed. Data collected with the CMS experiment in 2016 with an integrated luminosity of $35.9\,\text{fb}^{-1}$ was used.

As the invariant mass distribution of the electron and the muon without any signal-specific analysis cuts showed no significant deviation between the recorded data and the estimated Standard Model background, it served for calculating an upper limit of 2.22 on the pre-exponential factor, which denotes the fraction of quark-quark interactions above the sphaleron energy threshold of 9 TeV that undergo sphaleron transitions.

Requiring equally electrically charged leptons and more than six jets in the final state could on the one hand drastically improve the signal to background ratio, but raised issues on the adequate background simulation on the other hand. The used MC samples probably fall short of correctly simulating quantities like the misidentification rate of the lepton's charge. Besides that, there could be other SM processes that have been wrongly neglected for these specific selection criteria.

It was shown that further searches for sphalerons at the LHC could be worthwhile, as the statistical potential of setting lower exclusion limits on the pre-exponential factor is certainly given.

Bibliography

[1] Wolfgang Demtroeder. *Experimentalphysik 4*. Springer Spektrum, 2017.

[2] The Standard Model of elementary particles. https://en.wikipedia.org/wiki/Standard_Model#/media/File:Standard_Model_of_Elementary_Particles.svg, 2006.

[3] LHCb Collaboration. Observation of $J/\psi\phi$ Structures Consistent with Exotic States from Amplitude Analysis of $B^+ \to J/\psi\phi K^+$ Decays. https://link.aps.org/doi/10.1103/PhysRevLett.118.022003, Jan 2017.

[4] LHCb Collaboration. Observation of $J/\psi p$ Resonances Consistent with Pentaquark States in $\Lambda_b^0 \to J/\psi K^- p$ Decays. https://link.aps.org/doi/10.1103/PhysRevLett.115.072001, Aug 2015.

[5] A L Read. The discovery and measurements of a higgs boson. http://stacks.iop.org/1402-4896/2013/i=T158/a=014009, 2013.

[6] Frans Klinkhamer. Sphalerons in the Standard Model. https://www.rug.nl/research/vsi/events/groenewold/klinkhamer.pdf, Oct 2016.

[7] Daria Satco. Search for Sphalerons in Proton-Proton Collisions. https://cds.cern.ch/record/2278326, Aug 2017.

[8] Graham Albert White. *A Pedagogical Introduction to Electroweak Baryogenesis*. 2053-2571. Morgan and Claypool Publishers, 2016.

[9] S.-H. Henry Tye and Sam S.C. Wong. The Chern-Simons Number as a Dynamical Variable. https://arxiv.org/abs/1601.00418, 2016.

[10] S.-H. Henry Tye and Sam S. C. Wong. Bloch wave function for the periodic sphaleron potential and unsuppressed baryon and lepton number violating processes. https://link.aps.org/doi/10.1103/PhysRevD.92.045005, Aug 2015.

[11] John Ellis and Kazuki Sakurai. Search for sphalerons in proton-proton collisions. *Journal of High Energy Physics*, 2016(4), Apr 2016.

[12] CMS Collaboration. Search for black holes and sphalerons. https://arxiv.org/abs/1805.06013, 2017.

[13] Michael Dine and Alexander Kusenko. Origin of the matter-antimatter asymmetry. *Rev. Mod. Phys.*, 76:1–30, Dec 2003.

[14] James M. Cline. Der Ursprung der Materie. *Spektrum der Wissenschaft*, Oct 2004.

[15] Xabier Cid-Vidal and Ramon Cid. LHC: the emptiest space in the solar system. https://doi.org/10.1088/0031-9120/46/1/005, 2010.

[16] Philippe Mouche. Overall view of the LHC. https://cds.cern.ch/record/1708847/?ln=de, 2014.

[17] CERN. Accelerator Performance and Statistics. http://acc-stats.web.cern.ch/acc-stats/#lhc/overview-panel.

[18] CMS Collaboration. The CMS experiment at the CERN LHC. https://doi.org/10.1088/1748-0221/3/08/S08004, 2008.

[19] Lucas Taylor. Sectional view of the CMS detector. http://cms.web.cern.ch/news/cms-detector-design, 2011.

[20] F Ragusa and L Rolandi. Tracking at LHC. http://stacks.iop.org/1367-2630/9/i=9/a=336, 2007.

[21] David Barney and Marzena Lapka. ECAL Poster 2013. https://cms-docdb.cern.ch/cgi-bin/PublicDocDB/ShowDocument?docid=12172, 2013.

[22] C. Patrignani and Particle Data Group. Review of particle physics. http://stacks.iop.org/1674-1137/40/i=10/a=100001, 2016.

[23] Cameron Bravo and Jay Hauser. BaryoGEN, a Monte Carlo generator for sphaleron-induced transitions in proton-proton collisions. https://arxiv.org/abs/1805.02786, 2018.

[24] Hung-Liang Lai, Marco Guzzi, Joey Huston, Zhao Li, Pavel M. Nadolsky, Jon Pumplin, and C.-P. Yuan. New parton distributions for collider physics. https://link.aps.org/doi/10.1103/PhysRevD.82.074024, Oct 2010.

[25] CMS Collaboration. Baseline muon selections for Run-II. https://twiki.cern.ch/twiki/bin/viewauth/CMS/SWGuideMuonIdRun2#HighPt_Muon.

[26] CERN Collaborattion. Muon trigger and identification. https://cds.cern.ch/record/220657, 1990.

[27] CMS Collaboration. HEEP Electron ID and isolation. https://twiki.cern.ch/twiki/bin/viewauth/CMS/HEEPElectronIdentificationRun2.

[28] CMS Collaboration. Electron and photon performance in CMS with the full 2016 data sample. https://twiki.cern.ch/twiki/bin/view/CMSPublic/PhysicsResultsEGM, 2017.

[29] Physics Validation Group. Utilities for accessing pileup information for data. https://twiki.cern.ch/twiki/bin/viewauth/CMS/PileupJSONFileforData.

[30] CMS Collaboration. CMS Luminosity Measurements for the 2016 Data Taking Period. Technical Report CMS-PAS-LUM-17-001, CERN, Geneva, 2017.

[31] Juan Rojo. PDF4LHC recommendations for Run II. https://arxiv.org/abs/1606.08243v1, 2016.

[32] PDF4LHC group. PDF4LHC recommendations for LHC Run II. http://stacks.iop.org/0954-3899/43/i=2/a=023001, 2016.

[33] CMS Collaboration. Dielectron resonance search in Run 2 at $\sqrt{s} = 13\,\text{TeV}$ pp collisions. Technical Report CMS-AN-2015/222, CERN, 2015.

[34] CMS Collaboration. Search for new physics in the lepton and MET final state with 2016 data. Technical Report CMS AN-16-204, CERN, 2017.

[35] CMS Collaboration. Search for new physics, focused on W' production, in the single electron/muon plus missing-Et final states using pp collision data at $\sqrt{s} = 13\,\text{TeV}$. Technical Report CMS-AN-2015/266, CERN, 2015.

[36] CMS Collaboration. Search for lepton flavor violating decays of heavy resonances to $e\mu$ pairs in pp collisions at $\sqrt{s} = 13\,\text{TeV}$. Technical Report CMS-AN-16-163, CERN, 2018.

[37] Michelangelo L. Mangano, Mauro Moretti, and Roberto Pittau. Multijet matrix elements and shower evolution in hadronic collisions: $wb\bar{b}$+n-jets as a case study. `http://www.sciencedirect.com/science/article/pii/S0550321302002493`, 2002.

[38] Mark Olschewski. Search for new physics in proton-proton collision events with a lepton and missing transverse energy. `http://publications.rwth-aachen.de/record/572409`, 2016.

[39] CMS Higgs Physics Analysis Group. Documentation of the RooStats -based statistics tools for Higgs PAG. `https://twiki.cern.ch/twiki/bin/viewauth/CMS/SWGuideHiggsAnalysisCombinedLimit`.